General Disclaimer

One or more of the Following Statements may affect this Document

- This document has been reproduced from the best copy furnished by the organizational source. It is being released in the interest of making available as much information as possible.

- This document may contain data, which exceeds the sheet parameters. It was furnished in this condition by the organizational source and is the best copy available.

- This document may contain tone-on-tone or color graphs, charts and/or pictures, which have been reproduced in black and white.

- This document is paginated as submitted by the original source.

- Portions of this document are not fully legible due to the historical nature of some of the material. However, it is the best reproduction available from the original submission.

9950-1036

(NASA-CR-175688) STRESS AND EFFICIENCY STUDIES Quarterly Progress Report, 1 Oct. - 31 Dec. 1984 (Mobil Tyco Solar Energy Corp.) 28 p HC A03/MF A01 CSCL 10A

N85-24531

Unclas G3/44 21037

DOE/JPL 956312/10
Distribution Category UC-63

Mobil Solar Energy Corporation
16 Hickory Drive
Waltham, Massachusetts 02254

STRESS AND EFFICIENCY STUDIES IN EFG

Program Manager: Juris P. Kalejs

Quarterly Progress Report - Subcontract No. 956312

Covering Period: October 1, 1984 - December 31, 1984

Distribution Date: February 15, 1985

"The JPL Flat Plate Solar Array Project is sponsored by the U.S. Department of Energy and forms part of the Solar Photovoltaic Conversion Program to initiate a major effort toward the development of flat plate solar arrays. This work was performed for the Jet Propulsion Laboratory, California Institute of Technology by agreement between NASA and DOE."

DOE/JPL 956312/10
Distribution Category UC-63

Mobil Solar Energy Corporation
16 Hickory Drive
Waltham, Massachusetts 02254

STRESS AND EFFICIENCY STUDIES IN EFG

Program Manager: Juris P. Kalejs

Quarterly Progress Report - Subcontract No. 956312

Covering Period: October 1, 1984 - December 31, 1984

Distribution Date: February 15, 1985

"The JPL Flat Plate Solar Array Project is sponsored by the U.S. Department of Energy and forms part of the Solar Photovoltaic Conversion Program to initiate a major effort toward the development of flat plate solar arrays. This work was performed for the Jet Propulsion Laboratory, California Institute of Technology by agreement between NASA and DOE."

Jet Propulsion Laboratory
California Institute of Technology
4800 Oak Grove Drive
Pasadena California 91109
(818) 354-4321

JPL

May 3, 1985

NASA Scientific and Technical
Information Facility
P.O. Box 8757
Baltimore-Washington International Airport
Maryland 21240

Attn: Acquisitions Branch

Gentlemen:

Enclosed for your system input and for listing in STAR are two copies of the following subcontractor reports:

Contract No.	Corporate Source	Report No.	File No.
956786-1	Westinghouse R&D Center	1st Qtr.	9950-951
956615-4	Westinghouse R&D Center	Qtrly.	9950-986
957031-1	Purdue Research Fdtn.	Qtrly.	9950-1002
956766-02	Wilkes College	2nd Qtr.	9950-971
955190	General Electric	Final	9950-912
955591-11	University of Toronto	Annual 1983	9950-985
956525-5	University of Florida	Qtrly.	9950-989
956349-01	Solavolt International	Final Design	9950-968
956335-1	Mobil Solar Energy Corp.	Final	9950-977
955782	Gould, Inc.	Mod. #5	9950-970
956614	Univ. of Washington	Annual 9-1-83 to 8-31-84	9950-1001
WO8746-83-1	Solar Energy Res. Inst.	Qtrly. 7/15/83 -10/15/83	9950-909
956797/02	SPIRE	Qtrly. No. 2	9950-969
956477	Univ. of Wisc. - Madison	Final	9950-1011
956785	Westinghouse R&D Center	3rd Qtrly.	9950-1010
956841	MIT	3-21 to 5/20/84	9950-1021
956541	HR Textron, Inc., Systems Eng. Div.	Extension Final	9950-1023
956797	SPIRE	Qtrly. No. 3	9950-1025
956042	TRW	Final Test	9950-1027
956384	Dynamics Research Corp.	Technical	9950-1030
955637	Dynamics Research Corp.	Final	9950-1029

Contract No.	Corporate Source	Report No.	File No.
*955637	Ford Aerospace & Comm. Corp	Test	9950-995
956722	Ford Corp.	FR	9950-1048
956885	RDA Logicon	FR	9950-1047
956503	System Planning Corp.	FR	9950-1051
955678	University of Arizona	FR	9950-1052
*956457	Aerojet Tech Systems Co.	Final	9950-974
956428	Arizona State University	FR	9950-1026
956525	Univ. of Florida	Qtrly.	9950-1033
956831-3	Arco Solar, Inc.	Qtrly.	9950-1035
956064	SRI International	Final	9950-1062
956042	TRW	Final	9950-1070
956038	Hughes Aircraft Co.	Final	9950-1069
956909	Earth Satellite Corp.	Final	9950-1078
954349	Thermo-Electron Corp.	Final Technical	9950-1080
956312	Mobil Solar Energy Corp.	Qtrly. 10/1 - 12/ 31/84	9950-1036

Very truly yours,

Arlene Ann Rush
Document Review Group
Documentation Section

AAR:dk

Enclosures
cc: P. French
Acquisitions Branch

*One copy only being sent.

ABSTRACT

Optical and electrical characterization of defects has been started in EFG ribbon grown in a system that will be used to test the stress model. Temperature and stress field modeling aimed at defining low stress growth configuration is also in progress, and results will be used to guide development of the experimental system.

The baseline defect configuration for ribbon grown at speeds of ~1 cm/min consists of dislocation densities of the order of 10^5 to $10^6/cm^2$, as well as saucer-type etch pits and line defects. All these defects are inhomogeneously distributed. EBIC measurements indicate that diffusion lengths are in the range 20-60 microns, and significant spatial inhomogeneities occur through the ribbon thickness. Growth speed changes in the range 0.7-1.0 cm/min do not produce significant variations in ribbon defect configurations.

TABLE OF CONTENTS

I. INTRODUCTION

The study of stress-generating mechanisms and means to reduce stress in high speed silicon sheet growth has been broadened to the examination of the electrical activity of dislocations and their influence on minority carrier diffusion length, and of the effect of deliberately added impurities, viz., common dopants, on dislocation and defect structure. The main approach of these added tasks is to attempt to identify the effects of plastic deformation through its impact on dislocation electrical activity by comparing of deliberately stressed FZ and CZ silicon with as-grown EFG sheet. The latter will be produced in a new EFG system designed to provide added flexibility for manipulation of thermoelastic stress levels during growth.

Several developments in the understanding of mechanisms of plastic deformation and of stress generation in high speed EFG growth of silicon sheet have produced information that can be used to construct new models for studying means to minimize stress during growth. Thermoelastic stress analysis clearly predicts that stress buildup in silicon sheet will lead to significant creep, buckling and residual stress of a magnitude sufficient to produce fracturing during cutting at room temperature. Experimental observations at a qualitative level on EFG sheet indicate that the residual stress is not of the magnitude expected from the thermoelastic theory. Creep response studies at high temperatures (1200-1400°C) show that silicon behaves essentially as a plastic solid even at moderate stress levels above the yield point stress (5-15 MPa), which are well below maximum predicted thermoelastic stresses (> 100 MPa). Dislocation densities of the order of $1 \times 10^7/cm^2$ have been generated in very short (< 10 sec) times in four-point bending experiments carried out up to strain rates ($\sim 10^{-3}$ s^{-1}) and strains ($\sim 10^{-2}$) expected to be representative of those produced by thermoelastic stress during sheet growth. Densities produced by steady-state creep are several orders of magnitude greater than this, and are usually never so high in as-grown sheet. In addition, secondary creep relationships deduced from the steady-state data and initially used in stress analysis predict creep rates that are orders of magnitude smaller at comparable stress levels than observed during the primary creep transients in the four-point bending experiments. These apparent differences can be reconciled for sheet growth

if it is assumed that most, if not all, dislocations generated during very high (> 1200°C) temperature creep are annihilated or escape to the sheet surfaces because of favorable glide plane orientations (e.g., (111) planes intersect the sheet surfaces). The high temperature creep response is therefore determined solely by the rate at which dislocations move under the applied stress, and by dislocation interactions with impurities, twin boundaries or other defects. Further, residual stress and dislocations remaining in as-grown sheet must result mainly from stress relief at lower temperatures ($\leq$ 1000°C) where the dislocation velocities are no longer high enough to allow complete stress relief.

Several changes in modeling approaches are suggested that can test this scenario. Those being pursued now include study of stress relaxation effects in the lower temperature region ($\leq$ 1200°C), and the effect of transverse temperature gradients (in the sheet width dimension). An EFG test system for experimental study of the stress analysis model has been constructed. This system provides more flexibility for changing post-growth temperature profiles than the EFG cartridge system for 10 cm wide ribbon used in the earlier part of this program.

Two new tasks have been started to complement the stress model testing. Electrical characterization of EFG defect structure by EBIC is being used to develop means to quantitatively measure minority carrier diffusion length with resolution sufficient to study activity at dislocations. This approach will be useful to compare electrical activity of stress-induced dislocations deliberately produced in FZ and CZ silicon in four-point bending to that in as-grown EFG dislocation structures. This comparison will be directed at attempting to determine the temperature at which the most deleterious dislocations arise in the sheet.

A second new task is examining the effects of deliberately introduced impurities, specifically dopant atoms, on EFG sheet quality. It is commonly observed that significant degradation of cell performance arises in all more highly defected silicon material with increasing dopant levels (resistivities below about 1 ohm-cm for EFG sheet and Silso silicon used for solar cells). The studies of defect structure in progress center at present on optical microscopy examination of changes in defect structure and dislocation density with dopant level increases of such impurities as boron and gallium.

II. PROGRESS REPORT

Ribbon grown at 1 cm/min in an EFG system designed to test the stress model has been studied to define its baseline defect configuration and electrical properties. Growth variables examined have been the speed, doping density and variations in the afterheater influencing the cooling profile

Stress analysis has been continued using a simple monotonically decreasing temperature profile to define minimum stress growth configurations that may be experimentally achieved in this EFG test system.

A. Advanced System Design

1. Defect Characterization (M.C. Cretella and N.W. Marr)

The EFG ribbon produced from the new test system installed in Furnace 17 has been studied from several points of view. This ribbon has dislocation densities that are much lower than those typical in growth at 3 cm/min in the EFG cartridge system for 10 cm wide ribbon. This offers an opportunity to study factors that may lead to changes in dislocation density from baseline levels. Initially, two factors were evaluated: dopant impurity effects and growth speed changes that may reduce the dislocation densities still further. All the ribbon grown is in the speed range of 0.6 to 1.0 cm/min at present. Growth speeds will be increased to above 1.0 cm/min later when minimum stress and defect density growth configurations have been identified for the current system.

Three types of defects are generally observed in EFG ribbon cross sections etched with the usual Sirtl etch. These are illustrated in the cross-sectional photomicrographs of undoped ribbon in Fig. 1. Dislocation etch pits are distinguished by their regular geometric shape and relatively deep etching. These may be rectangular or more triangular in shape. The first figure (1(a)) shows the pits at a low magnification after a normal 30-second etch; Fig. 1(b) is after an additional 30 seconds, which further develops the dislocation pit size. The region around the central vertical boundary, near the bottom of Fig. 1, is shown at a higher magnification in Fig. 2. This shows the second type of easily recognizable etch feature in EFG material, a smaller shallow pit quite distinct from the larger more regular dislocations. The density of these etch features quite clearly changes in traversing the boundary. This may be a result of orientation change, or signify that the underlying grain impurity content differs. It is planned to attempt to study these regions with the help of FTIR spectrophotometry, which could give indications if changes in carbon and oxygen concentrations are

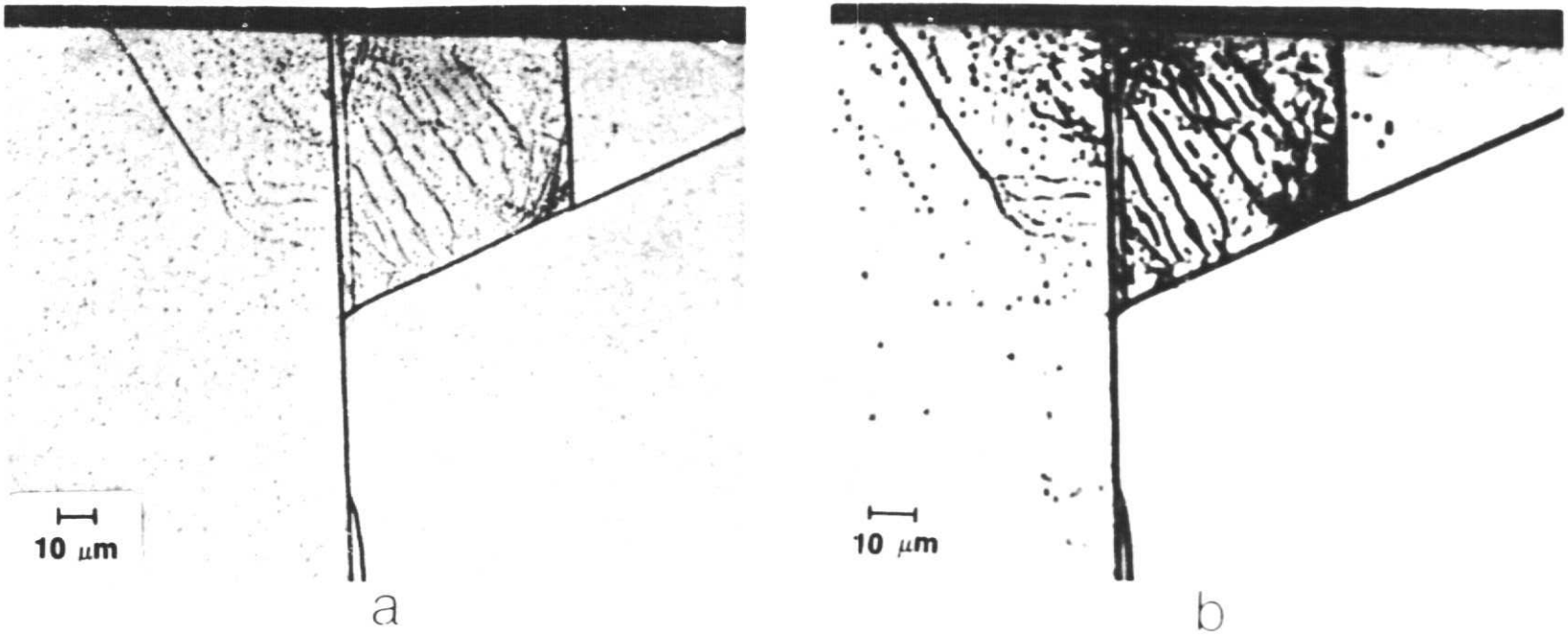

Fig. 1. Cross section micrcgraphs of undoped EFG ribbon Sirtl etched for (a) 30 s and (b) 60 s. Magnification 415X. Growth speed 0.6 cm/min.

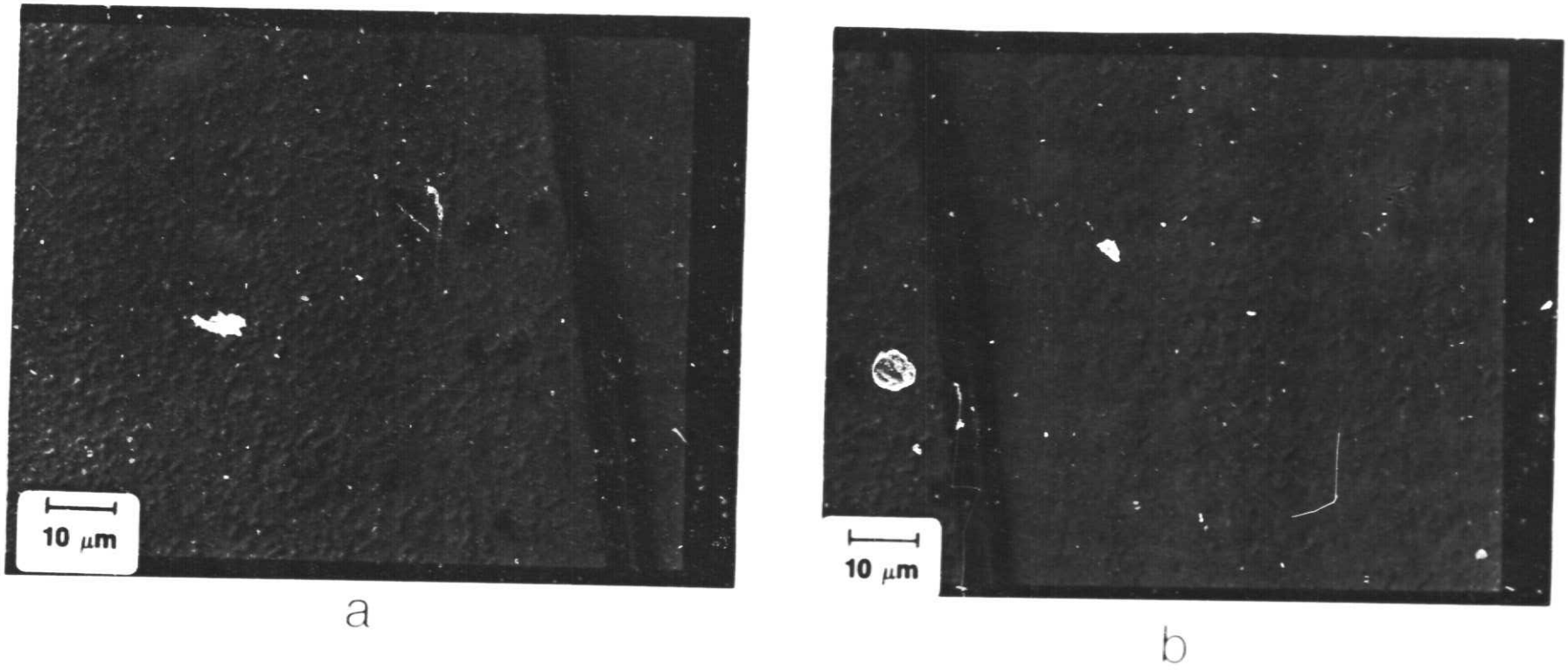

Fig. 2. High magnification (1100X) micrographs of central boundary region of Fig. 1(b) showing change in shallow etch pit density on left (a) and right (b) of boundary.

responsible for variations in the density of shallow etch pits. Since the grains which show these features often extend over distances many times the order of the ribbon thickness of 200-300 microns, this will be possible if sufficient resolution can be obtained.

The third common etch feature observed is illustrated in Fig. 3, where high magnification cross sections of a nominally undoped ribbon and one doped to about 0.5 ohm-cm with boron are compared. The undoped ribbon measured resistivities usually are in the range from 10-30 ohm-cm mainly as a result of residual boron in the charge material and crucible. The ribbon shown had an average measured resistivity of 8.6 ohm-cm. The main additional etch feature shown here is a line defect, which is quite distinct from the dislocations and shallow etch pits. There are no identifiable variations with boron level in the defect configurations and frequency of appearance of any of these three defects in evidence in this preliminary study of ribbon grown at 1 cm/min. More quantitative studies in this area are continuing. Indications from previous studies of EFG material grown at 2 cm/min are that increases in the dopant concentration tend to decrease the dislocation density and change the shape and density of the "line" defects. The average total density of the combined defects appears to remain constant, however.

Other dopants have also been introduced in order to observe if they produce significant defect configuration changes. Gallium and phosphorus have been used for this purpose. High magnification photomicrographs of the gallium-doped cross section are shown in Fig. 4 in high (~5 ohm-cm) and low (~0.2 ohm-cm) resistivity regions. Similarly, phosphorus-doped ribbon cross sections are shown in Fig. 5. The gallium-doped ribbon did not exhibit any identifiable changes in defect morphology. The etch pits in the phosphorus-doped ribbon appeared to develop differently and do not have as regular a shape as for dislocations in boron-doped material for equal etching times. This is typical of n-type silicon in general. However, no large-scale differences in defect density have been observed with changes in doping level or dopant type at a qualitative level. Further investigation will be directed toward attempting to reduce still further the dislocation density through manipulation of the post-growth temperature profile before dopant impurity effects are examined in more detail.

The variation of dislocation density with growth speed in the range from 0.7 to 1.0 cm/min has been studied in ribbon doped with boron to 1 ohm-cm. The microstructure in this ribbon is generally nonuniform, with large regions which are dislocation free, others with varying degrees of twinning (which have relatively low dislocation counts), and dislocated regions with densities between about 1×10^5 and $5 \times 10^6/cm^2$. The most dislocated regions appear usually in very localized bands, of the order of a few ribbon thicknesses in extent, and often have the appearance of previously identified Lüders bands.

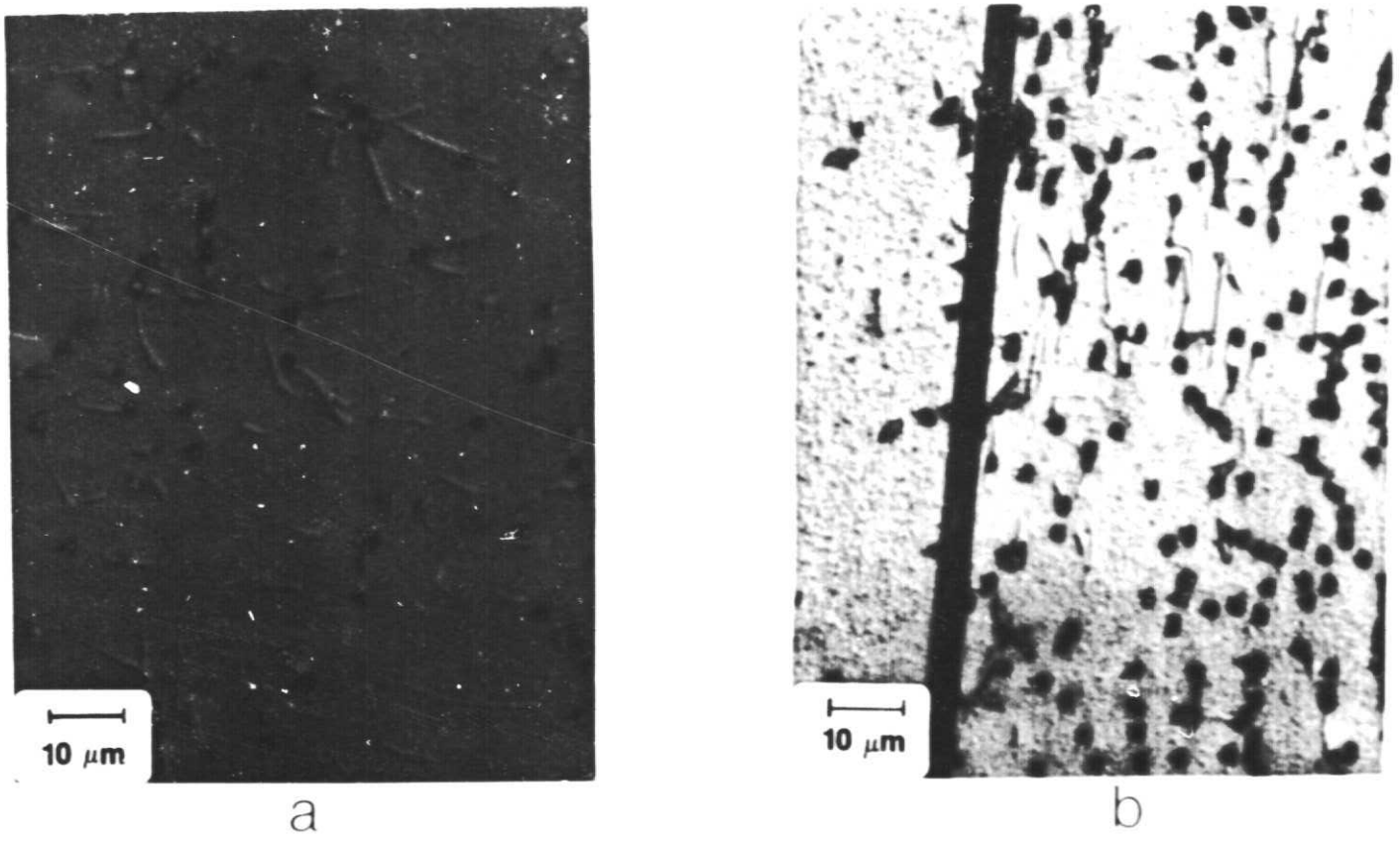

Fig. 3. Comparison of high resistivity (a) and low resistivity (b) boron-doped EFG material (1100X).

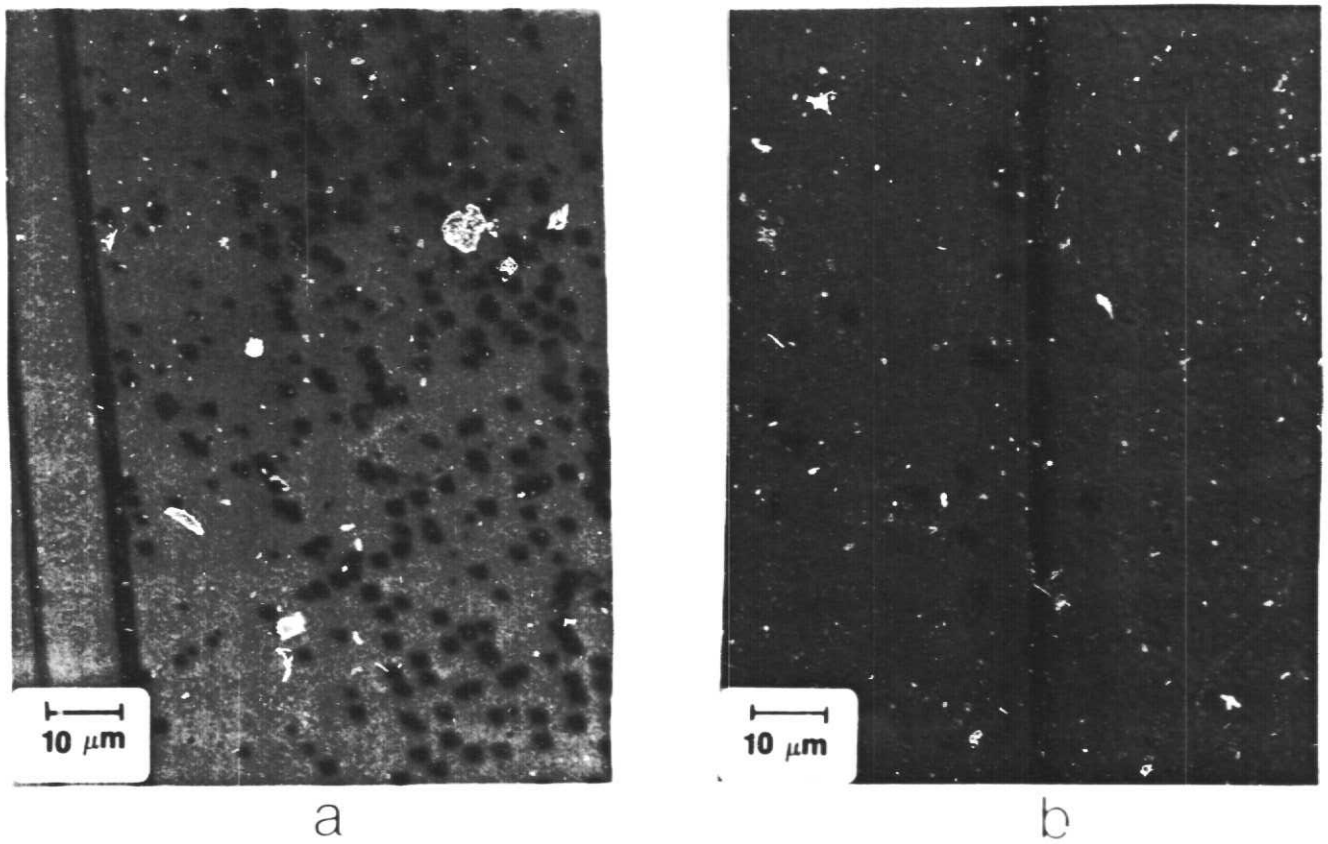

Fig. 4. High resolution (1100X) micrographs of cross sections of ribbon grown with gallium showing high resistivity (a) and low resistivity (b) regions.

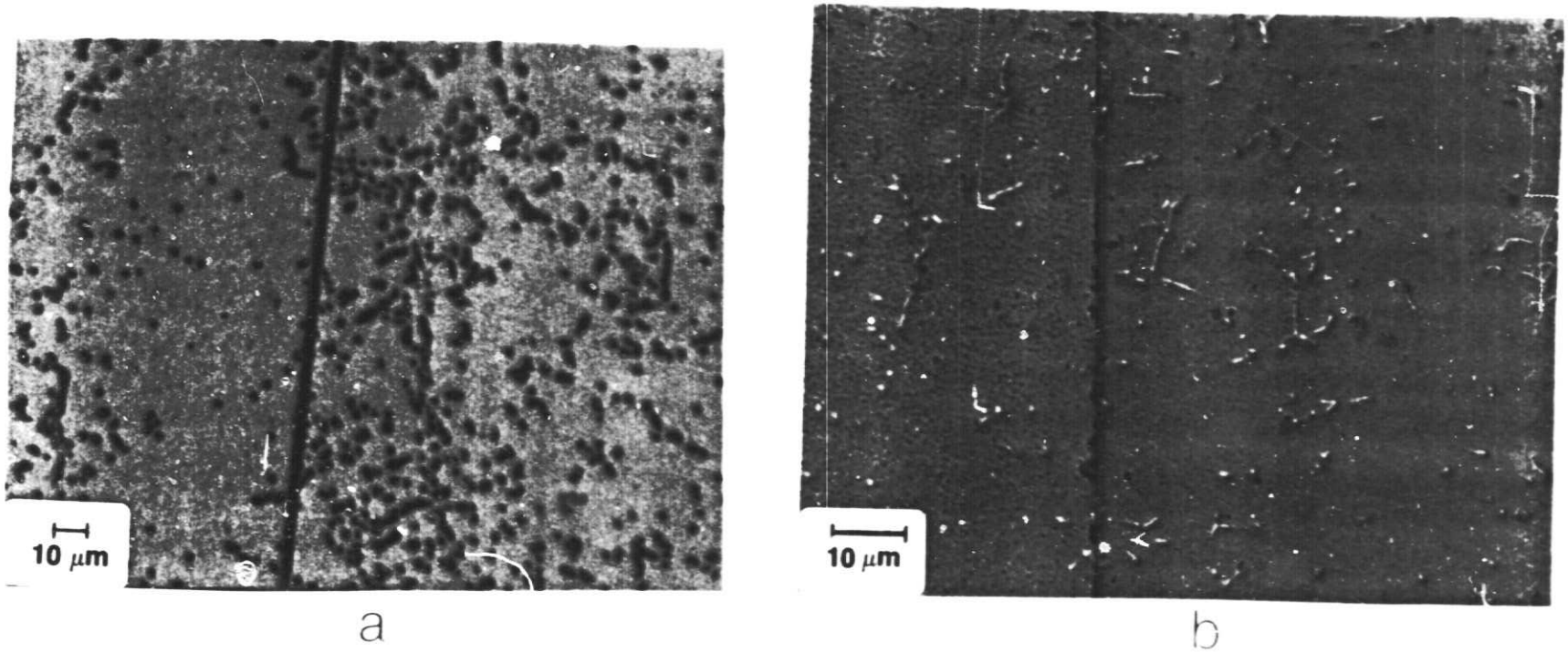

Fig. 5. Micrographs of cross sections of ribbon grown with phosphorus dopant at a level of about 0.5 Ω-cm: (a) phase contrast (415X); (b) normal light (1100X).

The dislocation counts were made using a video image analyzer attached to a high resolution optical microscope. The imaged field size is about 5 x 10^{-5} cm^2 (about 70 microns square) which represents a section of ribbon that is still a small fraction of a typical ribbon width (~300 microns). Because of the dislocation density inhomogeneities, the density can vary by orders of magnitude even through the ribbon thickness. Thus, the numbers obtained represent maximum and average values for highly localized regions of the ribbon, and the overall dislocation density, when taken over larger sections of the order of the ribbon thickness, will usually be lower.

The changes in extreme values of dislocation density with growth speed are given in the table below. The variations are not considered significant. Thus, it appears that for the given growth configuration, growth speed is not a parameter that can be used to reduce the dislocation densities still further.

Table I. Dislocation density as a function of growth speed for typical average and highly dislocated regions in ribbon doped to 1 ohm-cm with boron.

		N_D ($/cm^2$)	
Ribbon No.	Growth Speed (cm/min)	Average	High
17-S-28-2	0.75	5.7 x 10^5	4.4 x 10^6
-3	0.85	9.4 x 10^5	5.7 x 10^6
-1	0.95	2.2 x 10^5	3.2 x 10^6

2. Experimental Crystal Growth (J.P. Kalejs, A.A. Menna)

A variable which influences the defect configuration in addition to the growth speed and the post-growth cooling profile. Even if the effects of concentration of a given impurity on defect configuration are not in evidence in one situation (i.e., for a given growth speed or cooling profile), it is anticipated that variations in these growth conditions may lead to situations where the dopant concentration will become a stronger parameter in determining the defect density and type as it starts to influence creep relaxation. As noted above, we have started to see evidence that there may be different relationships between dopant level and defect concentration in EFG systems which are optimized to grow at 2 cm/min and higher and in the system studied here. Thus, the interaction between impurities and the stress field and cooling rate need also to be explored in the study of defect configurations in as-grown material. At present, we intend to concentrate only on means to further decrease the dislocation density and increase homogeneity of the ribbon, and leave these other questions to a later date.

The ribbon characterized above was produced with an afterheater configuration consisting of two tapered blocks of graphite insulation, as described in an earlier report [1]. Attempts were made to further vary the post-growth cooling profile with this arrangement. The insulation blocks were moved vertically, thus varying the space between the die top and the bottom of the insulation; additionally, one side of the insulation was removed, producing a highly asymmetric system by opening up one entire surface of the ribbon to radiate to a lower temperature environment. In the first case, displacements of up to 1.5 cm in the vertical direction (which presumably significantly changed the interface gradient very near the growth interface) did not lead to significant changes in the dislocation density. In the second case, dislocation densities did increase significantly, thus indicating that they could be influenced by providing a more unfavorable cooling profile. However, this system did not allow the flexibility desired in manipulating the temperature profile above about 1 cm from the growth interface in a controlled way. Thus, a second shield configuration has been constructed. This consists of a stack of graphite shields, as shown in Fig. 6. The spacing and number of shields can be varied, providing a convenient way to quickly change the cooling profile. Initial tests showed that growth was possible with this configuration, and detailed investigation of the ribbon produced, as well as measurements of temperature profiles, is in progress.

3. Stress Analysis (P. Mataga and J.W. Hutchinson, Harvard University)

A parametric study has been started of the relationship between the post-growth temperature profile and stress distributions in the sheet. The aim is to define minimum stress configurations and to reproduce them in the EFG system described above so that various aspects of the stress model can be tested.

The stress analysis is carried out for an idealized sheet cooling temperature profile, as shown in Fig. 7. This consists of an initial exponentially decreasing region of temperatures and a linear region. This profile is represented mathematically by writing

$$T(x) = A \exp(-BX/L) + CX/L + D \quad (1)$$

The calculated profiles are parameterized by an interface gradient value (at X = 0), defined by

$$SO = T_M - T_R + A(B - 1)/L \quad (2)$$

and a room temperature gradient value (X = 20 cm)

$$SI = T_M - T_R - A/L \quad (3)$$

---

1. J.P. Kalejs et al., Quarterly Report, DOE/JPL 956312/08 (April 1, 1984 to June 30, 1984), August 15, 1984.

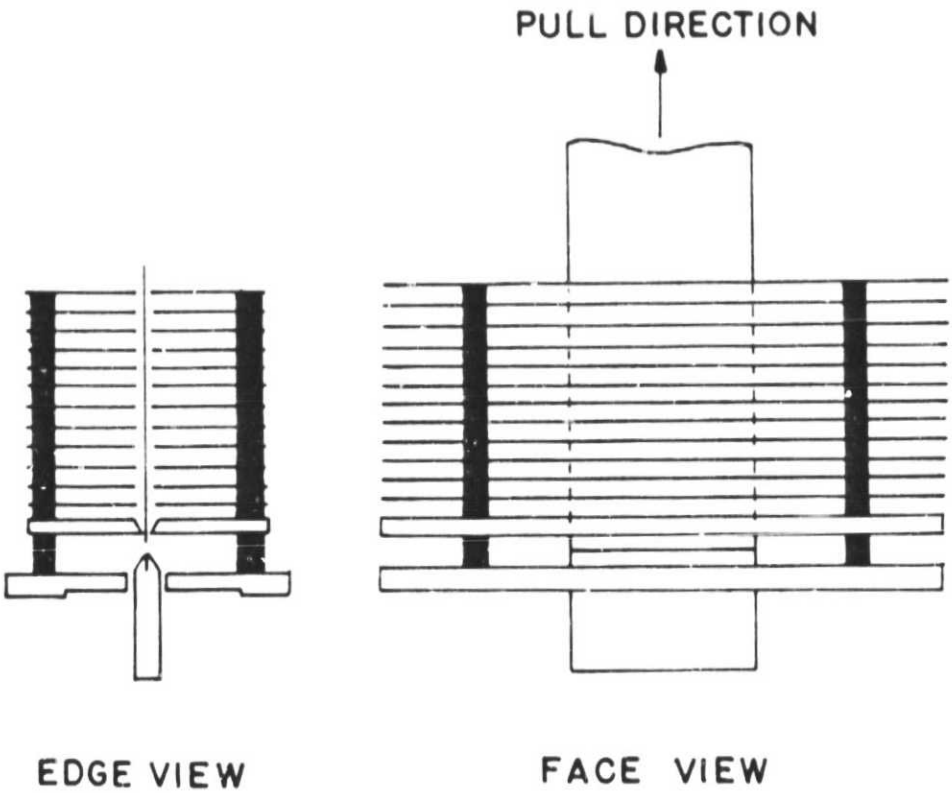

Fig. 6. Schematic of new shield configuration for EFG test system.

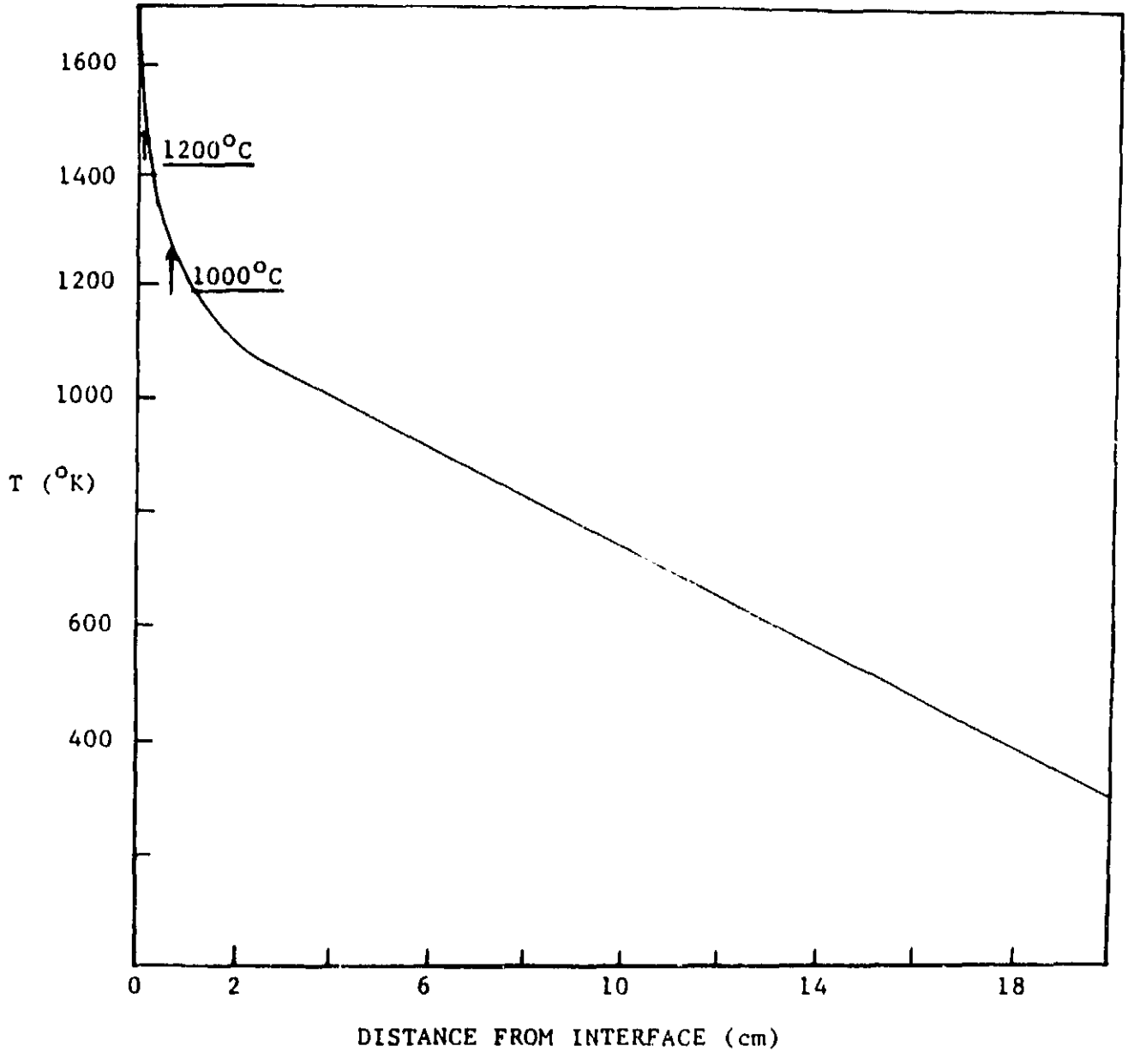

Fig. 7. Idealized monotonically decreasing temperature profile for high speed growth.

T_M and T_R are the interface (X = 0) and room temperatures, respectively. The calculations reported here all were carried out for a ribbon width of 5 cm, a growth speed of 3 cm/min and using the "high creep" representation defined in earlier work [1].

The value of representing the temperature profile by using the above parameters lies in the fact that the interface gradient, SO, defines the growth speed potential of the system, while the value chosen for the linearized region gradient, SI, will determine the point of intersection of the linear and exponential portions of the temperature profile. The approximate temperature region at which this occurs will in turn determine the impact of creep on residual stress. For example, it is expected from experimental creep data [1] that creep will be sufficiently rapid to relieve all stress above about 1200°C (see Fig. 7), while creep limitations will start to be manifested in the temperature region between 1200°C and 1000°C, provided growth speeds are of the order of or less than 3 cm/min.

The effect of varying the interface gradient from 500 to 1250°C/cm at a constant low temperature slope of 50°C/cm is shown in Figs. 8 and 9. In Fig. 9, the room temperature (residual stress) component σ_{xx} is plotted across the half-width of a 5 cm wide ribbon. These results can be compared to residual stress variations resulting from changes in the low temperature gradient value from 40 to 60°C/cm, as shown in Figs. 10 and 11. In the former case, as SO increases the nonlinear portion of the near-interface region of the temperature profile gradually moves away from the interface, from about 1-2 cm to over 4 cm, and the stress correspondingly increases. However, the stress variation is not large in comparison to that obtained in the second case. At a constant interface gradient parameter of 1000°C/cm, the increase of SO from 40 to 60°C/cm moves the nonlinear region of curvature from approximately 3 cm to less than 1 cm from the interface. The decrease in predicted room temperature stress is very large (Fig. 11), as σ_{xx} at the sheet edge drops from over 450 MPa to less than 100 MPa.

A further sensitivity analysis is given in Figs. 12 and 13. Here the impact of increasing SI from 50 to 60°C/cm at various values of the interface gradient SO is illustrated. A surprising result here is that ribbon edge stresses decrease with increasing interface gradient. This may be a real effect, but further investigation of the mathematics of the model is needed to rule out other causes. This is a concern because it can be seen from Fig. 12 that the transition from the high initial gradient to the linearized region now occurs within about 1 cm of the interface. In this region, stress and strain rate change very rapidly, and mesh size has been shown to influence convergence. A second approach to calculating stress components within the framework of the present analysis is also under investigation.

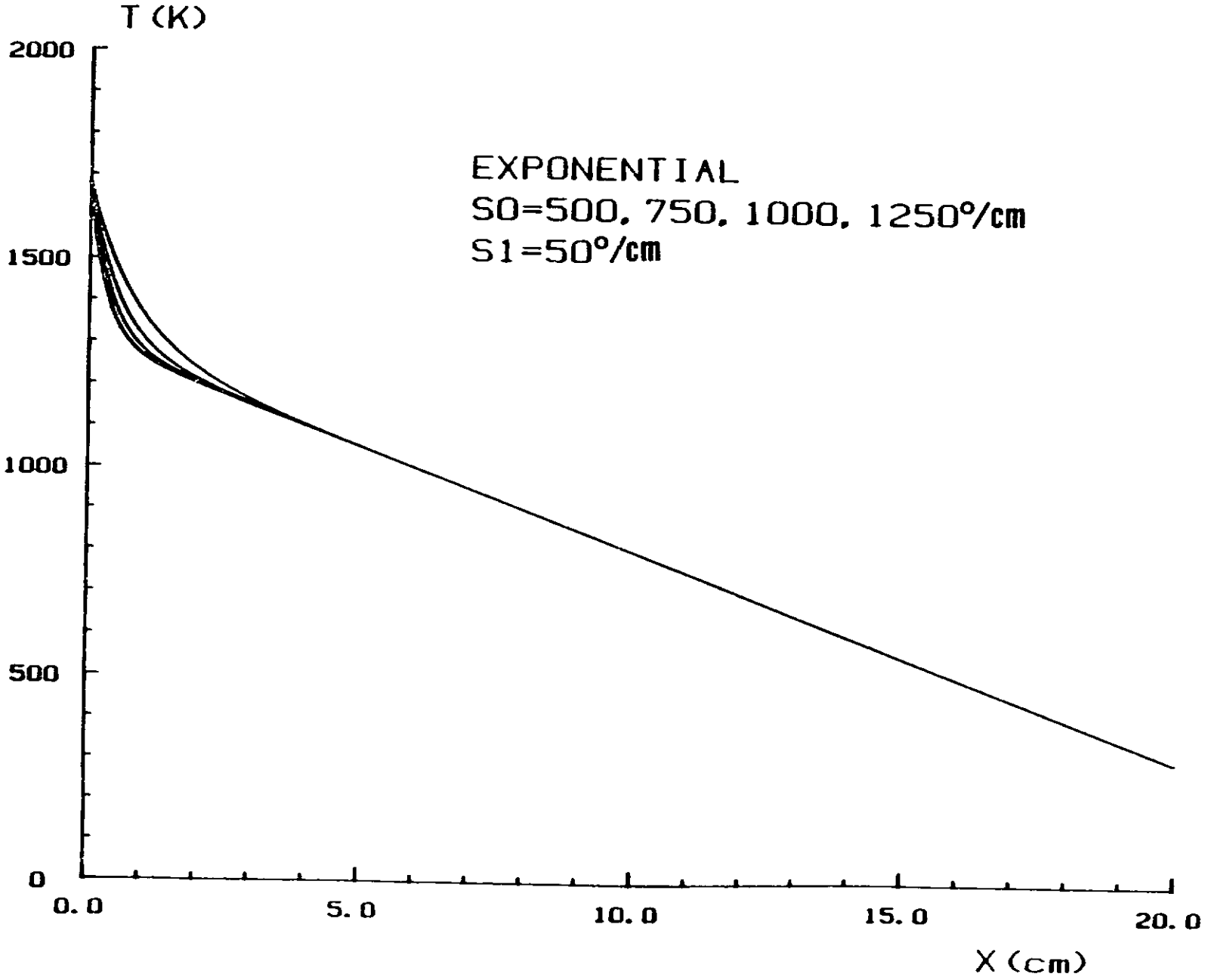

Fig. 8. Axial temperature profiles used for stress modeling with the interface gradient as variable.

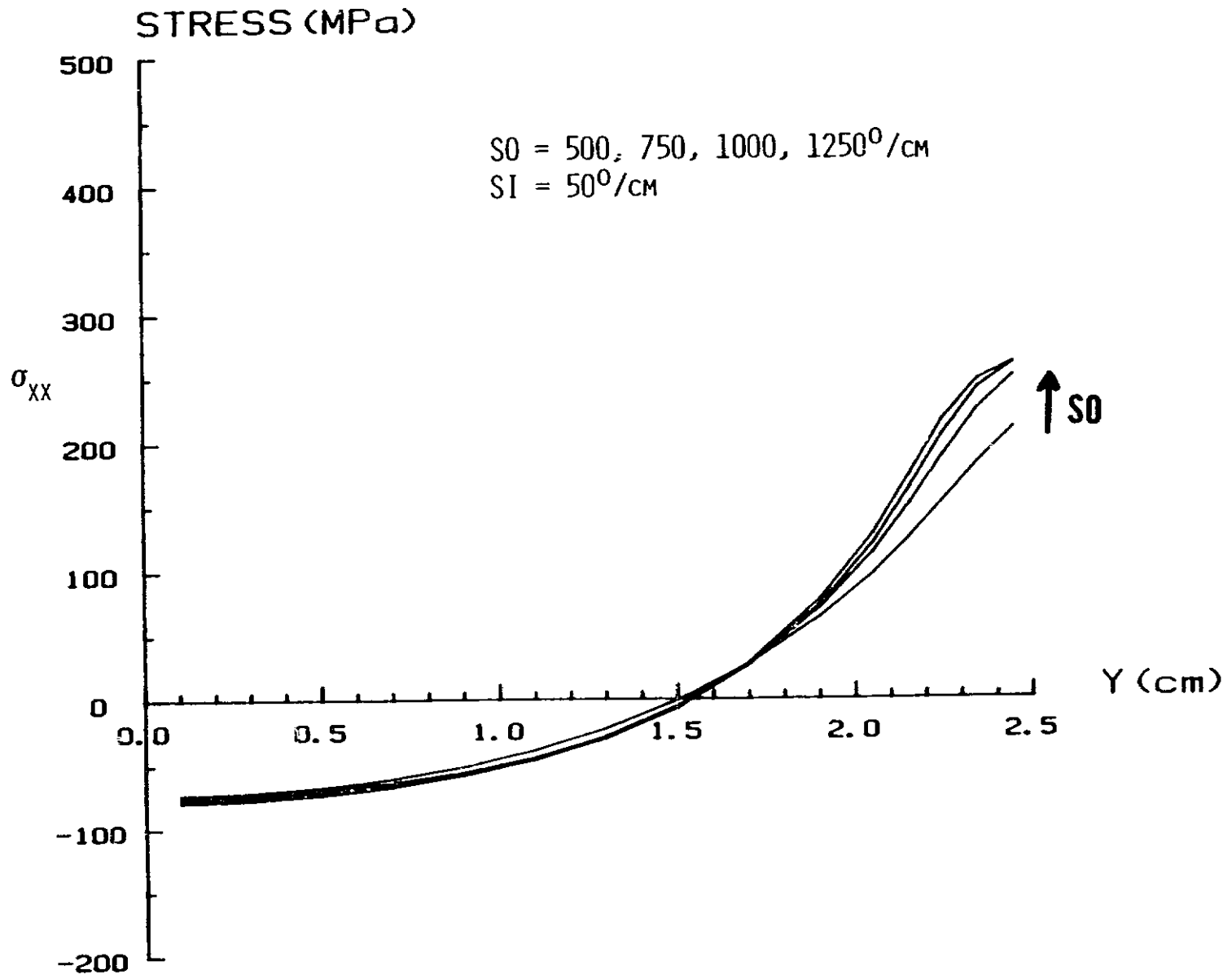

Fig. 9. Residual stress across sheet width for temperature profiles shown in Fig. 8.

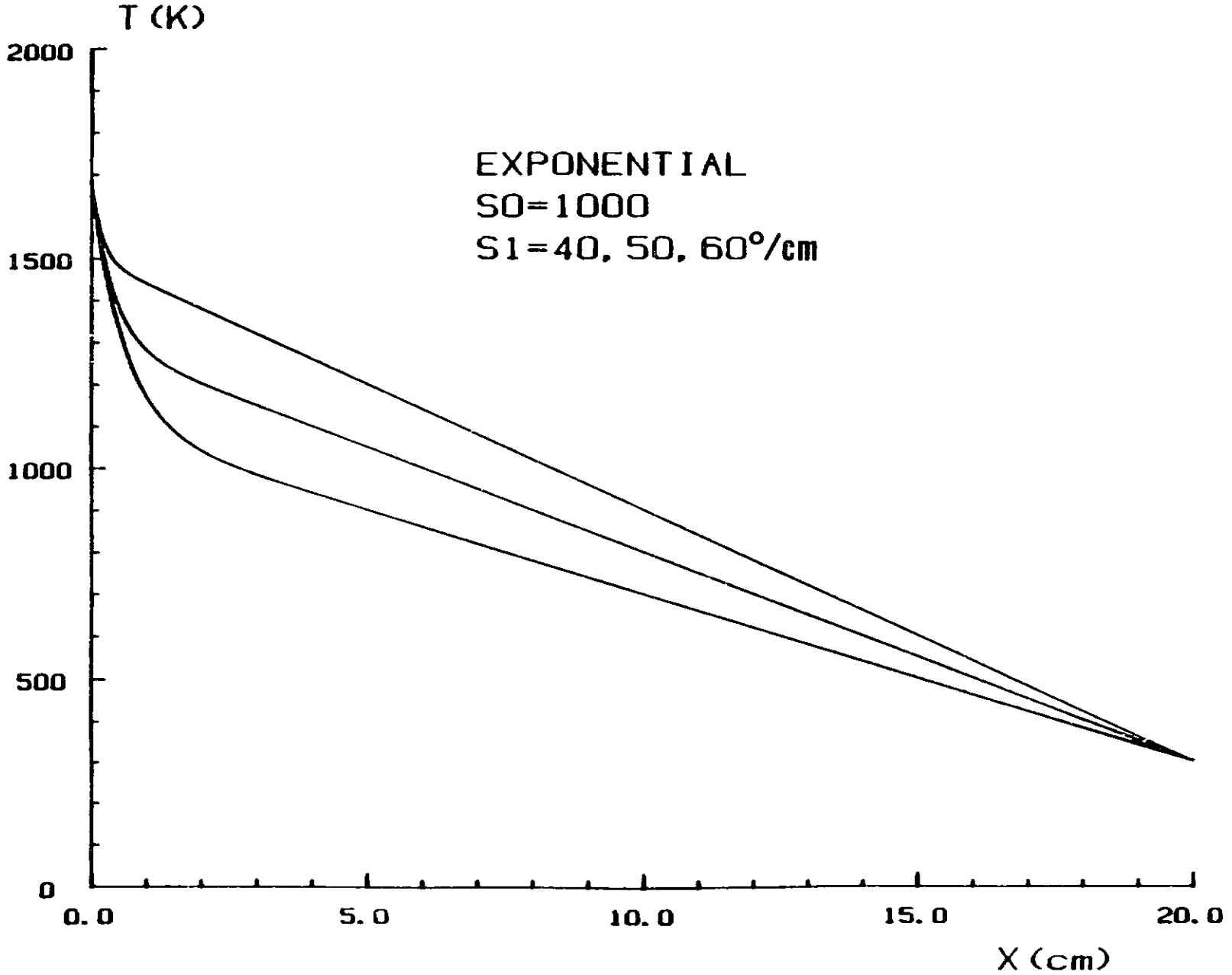

Fig. 10. Axial temperature profiles used for stress modeling with the linearized region gradient as variable.

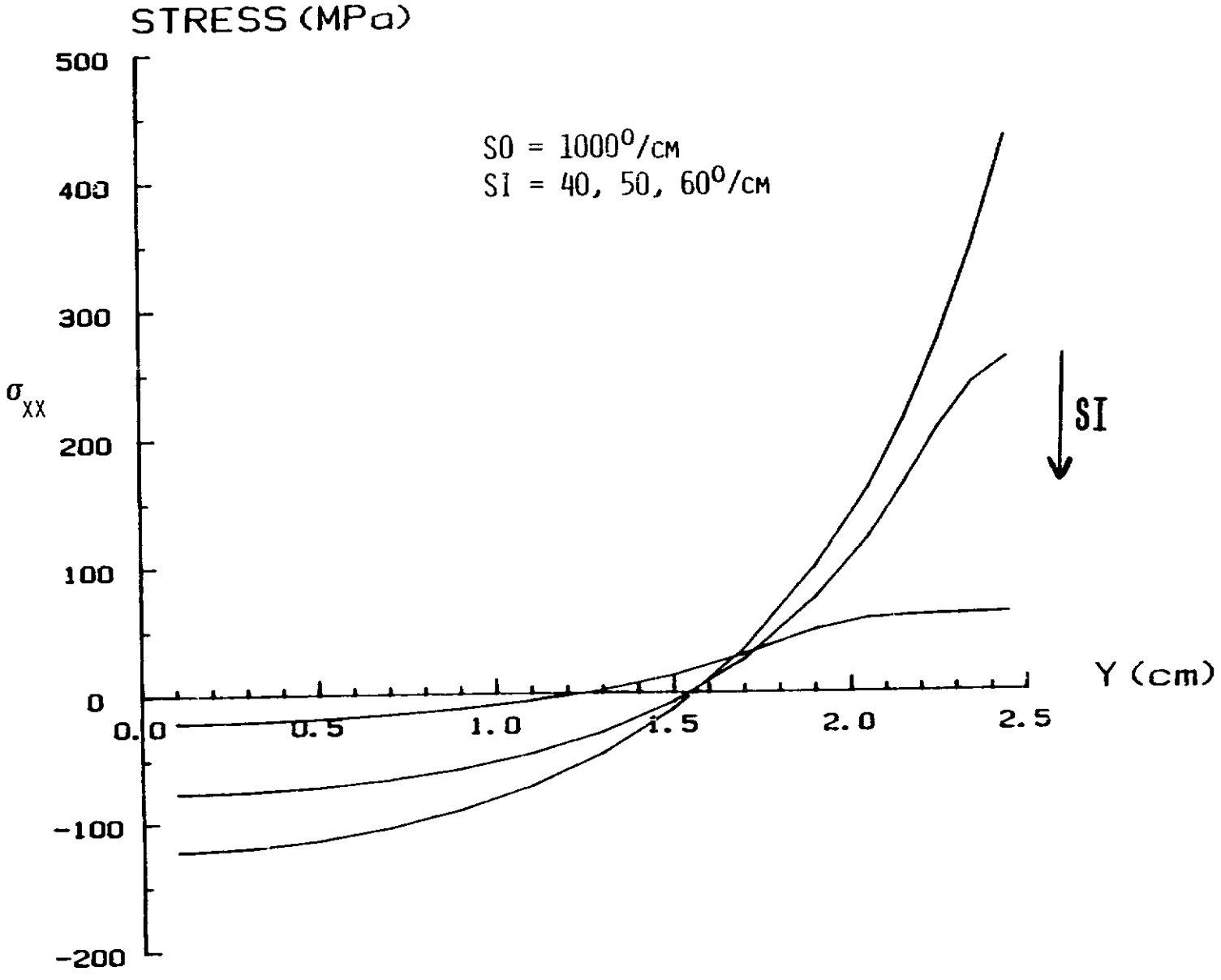

Fig. 11. Residual stress across sheet width for temperature profiles shown in Fig. 10.

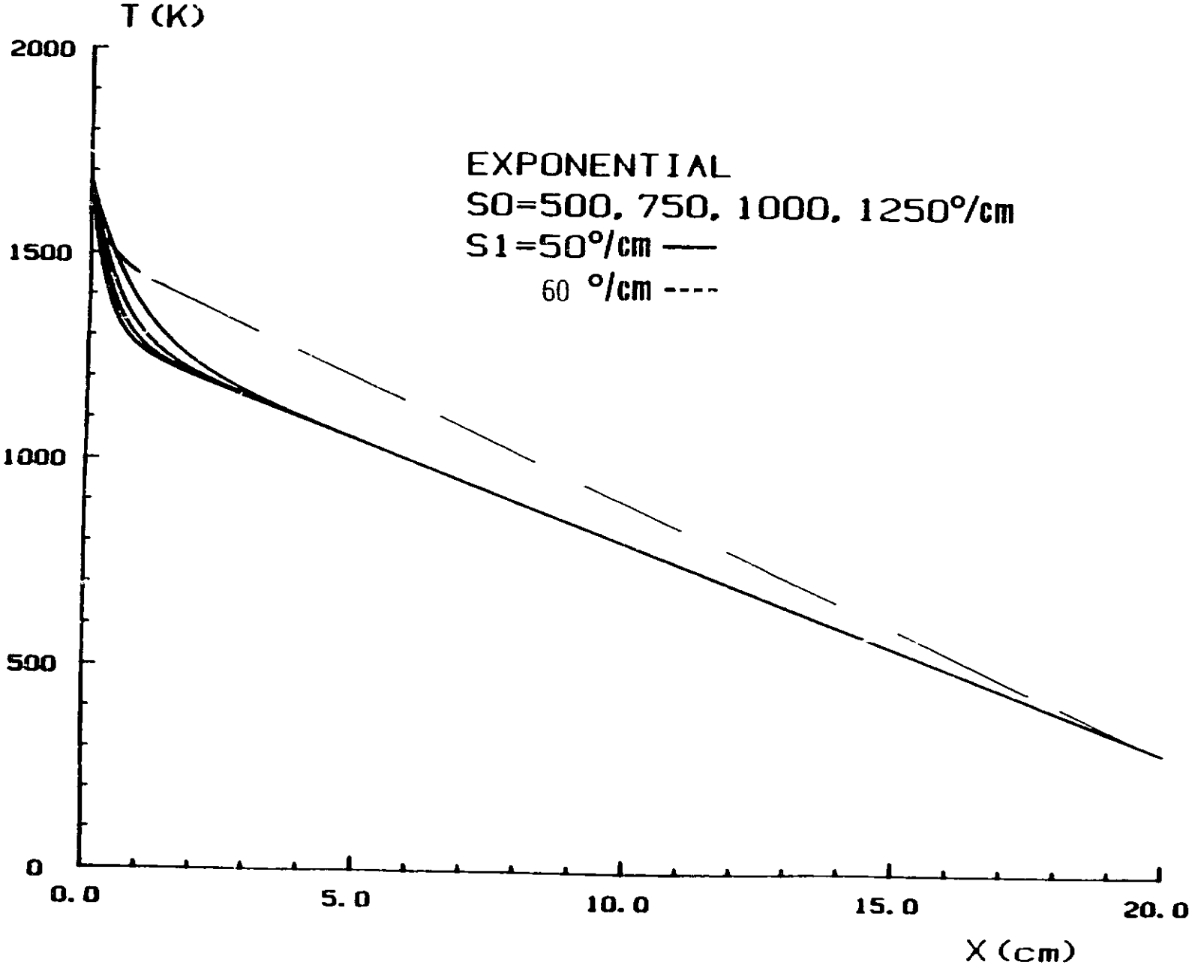

Fig. 12. Comparison of temperature profile with S0 = 1000°C/cm and SI = 60°C/cm (dashed line) to cases of variable S0 but with SI = 50°C/cm.

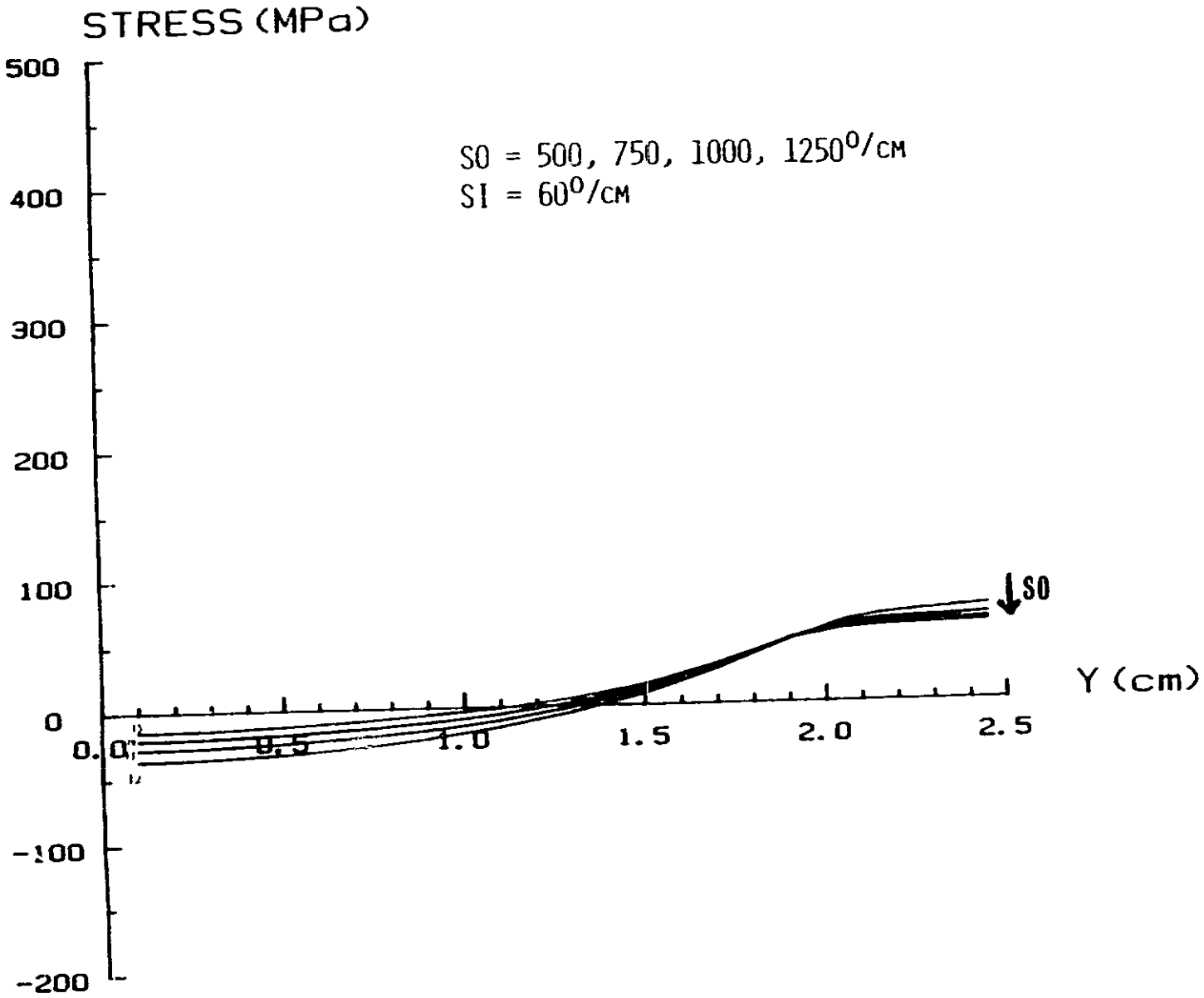

Fig. 13. Residual stress across sheet width for temperature profiles with constant linearized region slope SO = 60°C/cm and varying interface gradients.

B. Defect Electrical Characterization
(C. Dubé and D. Sandstrom)

EBIC study of EFG ribbon has been started. For this purpose, the ribbon grown in Furnace 17 and characterized above has been used. The ribbon was examined most extensively in cross section; that is, with the electron beam aligned parallel to the growth axis. This allows correspondence to be established between defect features observed in etching of ribbon cross sections, which is a typical way to study subsurface defect structure, and the EBIC current collection.

The room temperature EBIC response at 40 keV in terms of percent of collected current is traced out across two typical ribbon cross sections in Figs. 14 and 15. EBIC micrographs of the scan region and the current line scan are shown in the inset photograph. Variations of diffusion length with position across the ribbon thickness are of two distinct types. In Fig. 14, a dislocation-free region is scanned. The diffusion length values are assigned on the basis of calibrations established previously [1]. This trace shows that regions of higher diffusion length are found near the ribbon surfaces, with the lowest diffusion length occurring in the center of the ribbon cross section. This pattern mirrors the expected interface shape in that it generally is concave toward the melt, which leads to preferential impurity redistribution toward the centerline. In general, similar patterns are also observed in spreading resistance variations through the thickness.

The line scan in a region of the ribbon cross section where there is structure and dislocations is shown in Fig. 15. Now significantly sharper variations in diffusion length are observed to be superimposed on the same envelope, again on average producing higher diffusion lengths near the surface than near the centerline. More intense regions of recombinations associated with boundaries are also visible in this photomicrograph just outside of the region of the trace. Additional measurements have been done also on the surface of the ribbon. Numerical values of diffusion length obtained are in reasonable agreement with the cross section measurements. For the particular sample studied, the best cross-sectional diffusion lengths were in the range of 35 to 40 microns, while some values as high as 60 microns were obtained from surface barriers. Also, some regions were found where the cross-sectional traces were much flatter than those shown in Figs. 14 and 15. No attempt has been made to correlate the surface and cross section values of diffusion length at this time. The higher surface values found may indicate that an even greater degree of near-surface improvement than shown in Figs. 14 and 15 is achieved. It is possible that this is not reflected to the full extent in the measurements taken in cross section because barrier characteristics affect the collected current as the surface is approached in the data of Figs. 14 and 15.

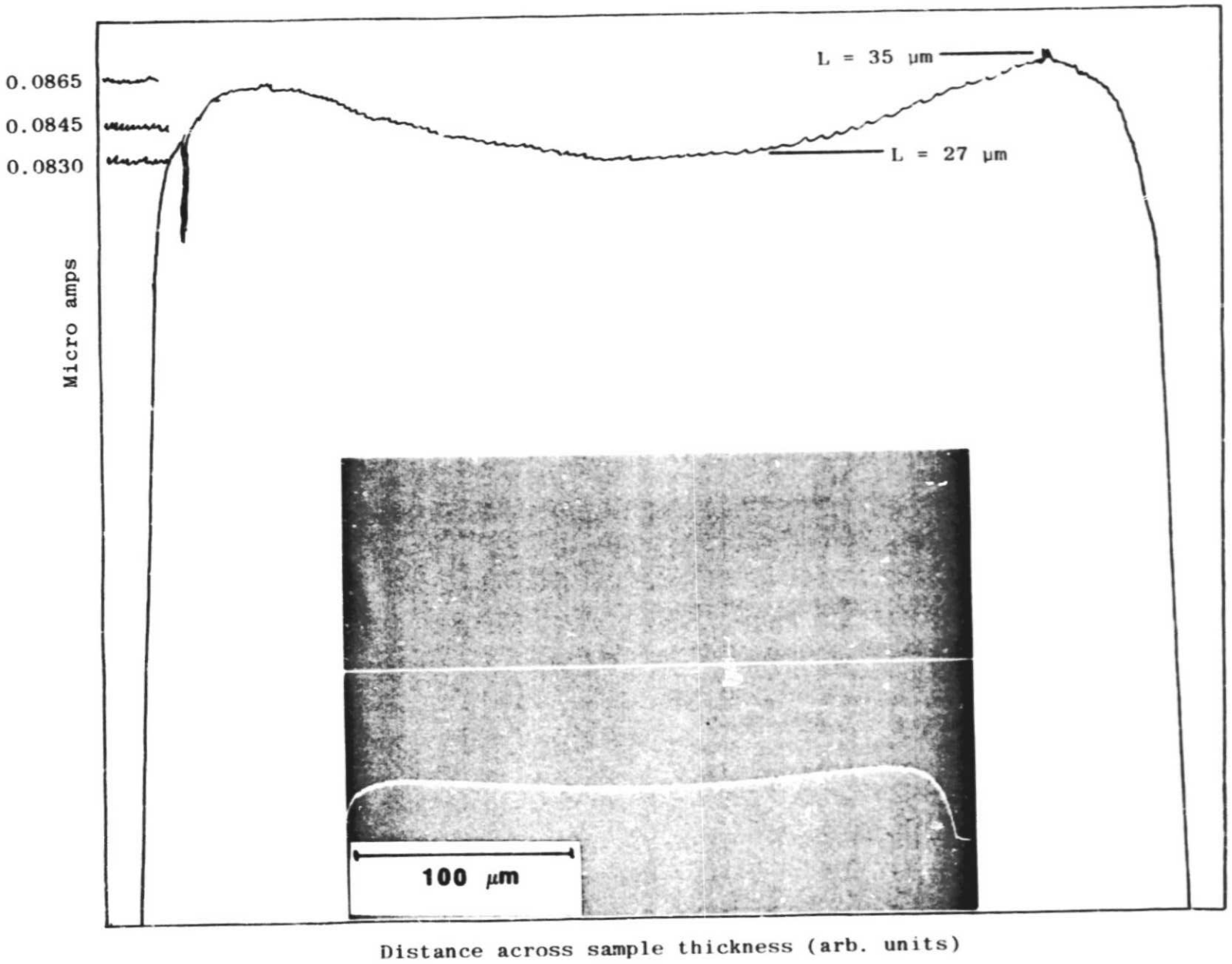

Fig. 14. High magnification (300X) room temperature EBIC line scan of EFG ribbon 17-S-20 in cross section for dislocation-free region.

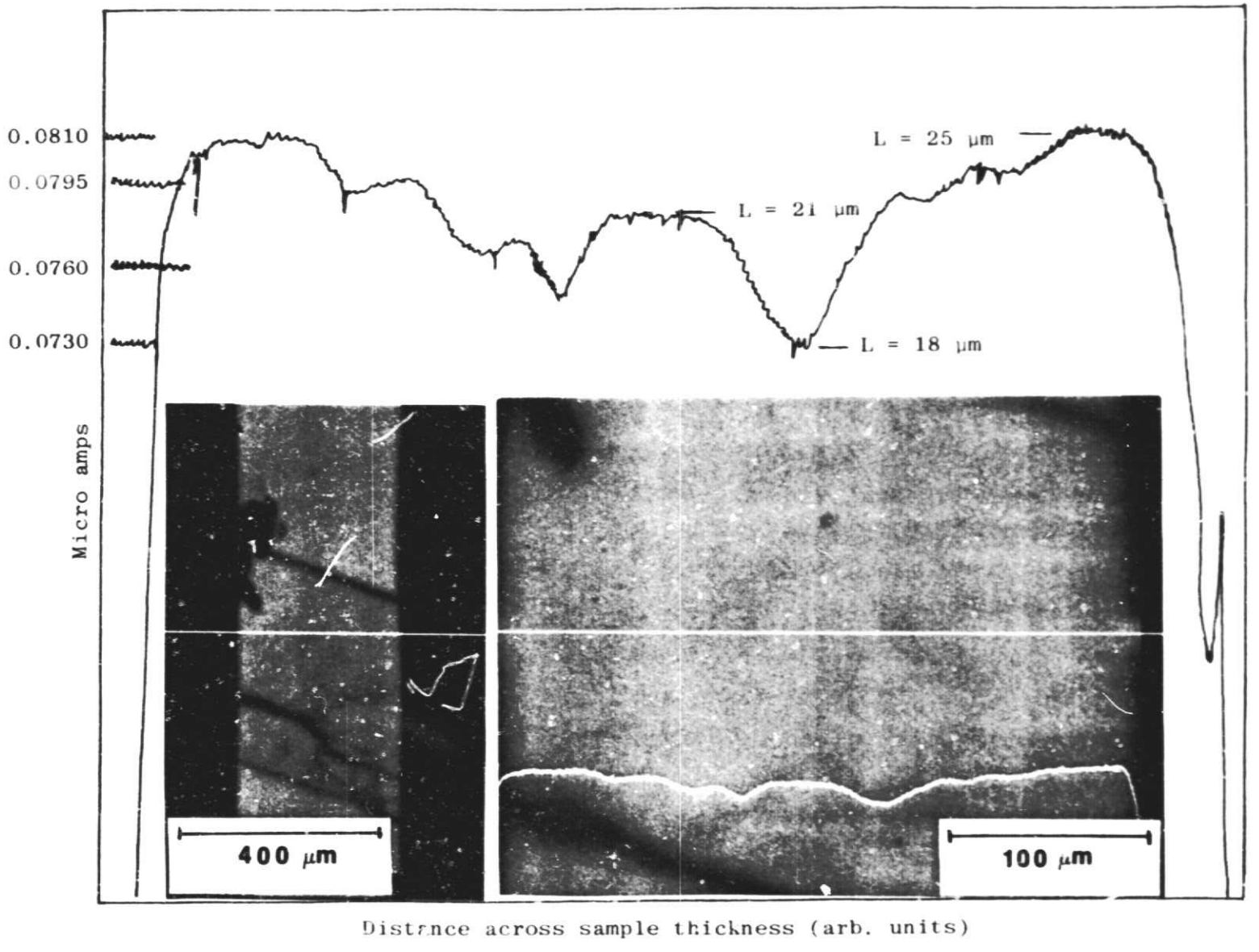

Fig. 15. High magnification (300X) room temperature EBIC line scan of EFG ribbon 17-S-20 in cross section for region with dislocations.

APPENDIX I

WORK BREAKDOWN STRUCTURE AND PROGRAM PLAN

September 1, 1984 - October 31, 1985

"STRESS AND EFFICIENCY STUDIES IN EFG SILICON"

SUBJECT	DESCRIPTION	'85 SEP	OCT	NOV	DEC	JAN	FEB	MAR	APR	MAY	JUN	JUL	AUG	SEP	OCT
Stress Analysis	Advanced system design concept testing to minimize stress.	X						X							
Efficiency	EFG defect electrical characterization.	X													X
Efficiency	Low resistivity sheet quality studies.	X													X
Program Management	Progress reports, etc.	X													X